(Received 12 June 2025, Accepted 18 July 2025, Scheduled 22 August 2025)

A Compact UWB Wearable Textile Antenna with Machine Learning Approach for IoT Applications

Khemchandra Anuragi and Pinku Ranjan*

ABV-Indian Institute of Information Technology and Management, Gwalior, M.P., India

ABSTRACT: This article presents a compact and flexible ultra-wideband (UWB) antenna with a defected ground structure (DGS) for IoT applications. The antenna is fabricated on a 0.7 mm thick jeans substrate to ensure high flexibility and take advantage of its universal availability. Machine learning (ML) techniques are applied to optimize the antenna's performance. A ring-shaped patch with DGS and C-type stubs is used to achieve a large bandwidth and reduce size. The total dimension of the proposed flexible antenna is $38\times26\times1.7$ mm^3. The primary aim of this article is to design a flexible UWB antenna with a remarkable impedance bandwidth of 131.45%, which covers frequencies from 2.56 GHz to 12.38 GHz. It operates at 3, 8, and 11.32 GHz frequencies with 99%, 98.30%, and 96.71% radiation efficiencies, respectively. The realized gain is 2.51, 3.70, and 5.46 dBi at frequencies 3, 8, and 11.32 GHz, respectively, with a peak gain of 5.46 dBi at 11.32 GHz. Specific absorption rate (SAR) values were tested using a human phantom and met FCC limits, confirming suitability for wearable and flexible IoT applications. The design was optimized using ML, with KNN performing best, achieving 99.5% accuracy in S-parameter prediction. The measured and simulated results are correlated with each other for flat and bent antennas.

1. INTRODUCTION

In recent decades, with the continuous advancement in wireless communication technology, many devices and gadgets have been connected to the internet [1, 2]. These different communication devices are interconnected and used in various applications through internet of things (IoT) networks [3]. The idea to design strong, flexible antennas that could be put on wearable or bending devices was accelerated by the variety of connected devices [4]. The system's performance is upgraded using accurate equivalent circuit models of the antenna, which may require complex mathematical analysis and simulation [5]. Because UWB devices provide fast transmission of information, extensive bandwidth, minimal energy utilization, encrypted communication, simple structure, and outstanding radiation performance, they could fulfill high connectivity demands [6, 7]. The Federal Communications Commission (FCC) permitted UWB applications to exploit the 3.1–10.6 GHz frequency spectrum in 2002, providing a 7.5 GHz overall bandwidth [8, 9]. Meanwhile, the Electronic Communication Committee has set aside the 6 to 8.5 GHz frequency band for UWB applications [10]. Due to their compact size and convenience, UWB antennas are essential to wireless body area networks (WBANs) and IoT devices [11]. These antennas are well suited for particular applications with inexpensive wireless sensors that need low-radiated power and stable data transmission [12]. Owing to their distinct properties, UWB antennas are well suited for integration into flexible and wearable IoT devices, enabling reliable and efficient wireless communication [13]. Textile materials are well suited for wearable antennas because of their mechanical flexibility and the comfort they offer to users [14].

The literature contains many UWB antenna designs on flexible substrates [15–19]. Praveena et al. designed a flexible antenna with full ground by using a flexible polydimethyl siloxane (PDMS) polymer substrate. Machine learning is used for validation, and the operates at 3.10–10.42 GHz range for wearable applications [15]. Desai et al. presented a polyethylene terephthalate (PET) substrate-based wearable antenna for IoT applications with a maximum gain of 2.49 dBi [16]. Lakrit et al. developed an elliptical antenna for wireless communications, which is Teflon-based and fed with a triple-band coplanar waveguide (CPW). DGS and split-ring resonators (SRRs) with circular shapes generate triple bands [17]. Das et al. presented a UWB antenna with circular polarization, which has dimensions of $75\times63\times1.52$ mm^3 and is printed over a Rogers RO4232 substrate. To achieve UWB performance, it uses an L-shaped feed and two L-shaped radiators [18]. This study introduces a circular UWB flexible antenna developed for IoT-based applications in the 2.56 to 12.38 GHz frequency band on a jeans substrate ($\varepsilon_r = 1.7$), with DGS ground. The jeans substrate minimizes the back radiation and obtains low SAR. The suggested flexible UWB antenna's overall measurements are $38 \times 26 \times 1.7$ mm^3, which confirms the antenna's compact form factor. Bandwidth enhancement techniques, including the incorporation of slots and stubs, are required to get UWB performance. Additionally, an ML-based approach is utilized to predict the antenna's return loss characteristics with improved accuracy.

The key contributions are addressed in the proposed antenna design.

* Corresponding author: Pinku Ranjan (pinkuranjan@iiitm.ac.in).

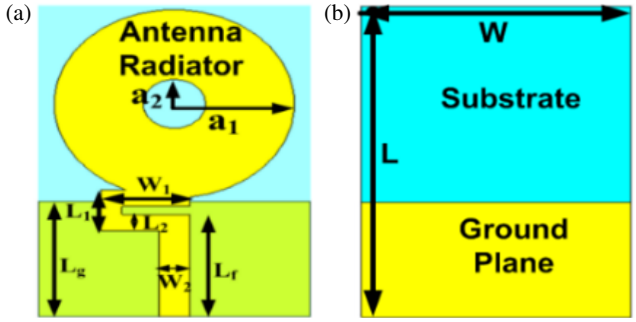

FIGURE 1. Layout of ring-shaped UWB antenna. (a) Plan view of layout, and (b) rear view. Physical specifications (Each element are in mm) are, $L = 38$, $W = 26$, $L_1 = 5$, $W_1 = 8.5$, $L_f = 12.5$, $W_2 = 3$, $L_g = 14.11$, $L_2 = 2$, $a_1 = 11.5$, $a_2 = 3$.

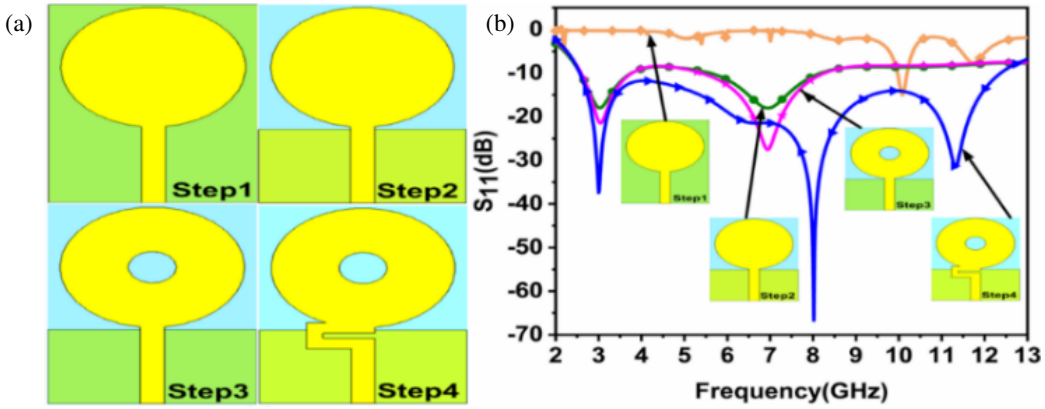

FIGURE 2. (a) Various evaluation steps. (b) Comparison between S_{11} for evaluation steps of UWB antenna.

- A novel and compact circular ring-shaped antenna achieving UWB with an impedance bandwidth of 131.45% (2.56–12.38 GHz) for $|S_{11}| < -10$ dB.
- An ML approach is used to predict S-parameters.
- A flexible thin jeans substrate is employed to reduce surface wave losses and enhance impedance matching, meeting wearable IoT antenna requirements.
- It provides a notable peak gain of 5.46 dBi at 11.32 GHz.
- The suggested antenna is ideal for wearable IoT applications since it reliably operates well under various bending scenarios in both free space and on-body conditions, with SAR values that are safely below FCC standards.

In order to examine the reflection coefficient (S_{11}), the suggested antenna is constructed and compared to the simulated ones. The following is a description of the paper's upcoming sections. Section 2 describes the antenna design, materials, evolution, and parametric study. Section 3 describes ML algorithm optimization, while Section 4 describes the practical outcomes. Section 5 presents the performance of the antenna in wearable IoT applications. The paper comes to an end in Section 6.

2. ANTENNA MODELING

2.1. Antenna Layout Aspects

Figure 1 illustrates the configuration of the proposed circular ring-shaped flexible textile antenna designed for wearable UWB applications. The antenna consists of a circular copper radiating patch with a thickness of 0.035 mm and a resistivity of $0.4 \times 10^{-5}\,\Omega \cdot$ m, fabricated on a 0.7 mm thick jeans fabric substrate. The substrate, with a relative permittivity (ε_r) of 1.7 and a loss tangent of 0.085, provides both flexibility and mechanical robustness. The ground plane is implemented beneath the substrate, acting as the lower conductive layer [6, 11]. The low dielectric constant of the fabric helps suppress surface wave losses and enhances impedance matching across the UWB range [19]. To improve bandwidth and impedance characteristics, a defective ground structure (DGS) and a C-shaped stub are incorporated into the design. The DGS disrupts the current path and enhances electromagnetic coupling, while the C-shaped stub positioned between the 50-Ω microstrip feed line and radiating patch modifies the current distribution and effective electrical length, leading to improved impedance behaviour. The antenna's evolution is shown in Figure 2(a), consisting of four design steps. Step 1 begins with a basic circular patch fed by a microstrip line, yielding a narrow bandwidth of 0.23 GHz (9.96–10.19 GHz), as shown in Figure 2(b). This limitation is attributed to high-Q geometry and limited current path

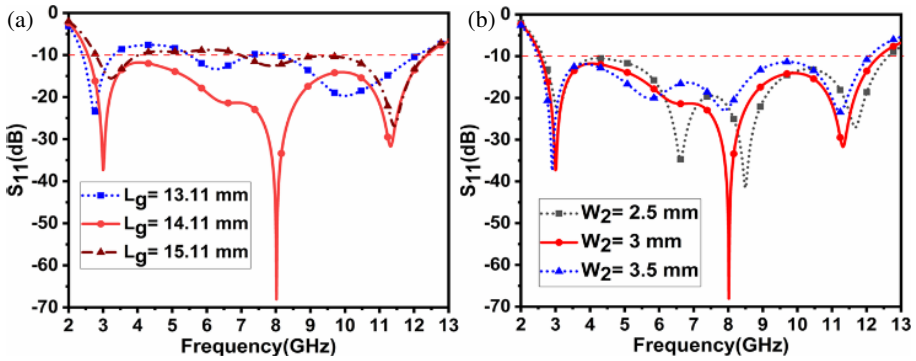

FIGURE 3. Comparison of simulated S_{11} for different values, (a) L_g, (b) W_2.

diversity. In Step 2, bandwidth is enhanced by trimming the ground plane to $14.11 \times 26\,\text{mm}^2$, resulting in dual-band operation (2.58–3.79 GHz and 5.61–8.18 GHz). Step 3 introduces a 3 mm radius circular ring slot to increase the electrical path and redistribute surface currents, which improves impedance matching. Step 4 integrates the C-shaped stub, which further increases the current path and provides reactive loading, enabling full UWB coverage. The final antenna structure, with dimensions of $26 \times 38 \times 1.7\,\text{mm}^3$ and a 12.5 mm long, 3 mm wide feed line, achieves efficient 50-Ω matching. The full design evolution and corresponding S_{11} results are presented in Figures 2(a) and 2(b), with optimized dimensions detailed in Figure 1.

According to Balanis [19], equations provided in [1, 20] are used to determine the antenna's dimensions. These values are subsequently fine-tuned to optimize the S_{11} response in Computer Simulation Technology (CST). The resonant frequency of the dominant mode, TM^Z, is calculated by the following equation.

$$(f_r) = \frac{1.8421\, v_0}{2\pi a_1 \sqrt{\varepsilon_r}} \tag{1}$$

where v_o is the light's free space velocity, a_1 the circular patch's radius, and ε_r the relative permittivity.

2.2. Parametric Study of Ring-Shaped UWB Antenna

A parametric study is crucial to better understanding the behavior of the antenna. It analyzes the impact of ground height and feed width variations.

2.2.1. Effect of Variation of Ground Plane (L_g)

Antenna impedance matching is more significantly impacted by ground layer variations at higher frequencies than at lower ones. Adjusting the size of the ground layer from 13.11 mm to 15.11 mm in 1 mm steps shows that the best impedance matching occurs when the ground plane is 14.11 mm, depicted in Figure 3(a). As a result, the ideal ground plane size is 14.11 mm, which offers a bandwidth of 9.82 GHz and ultra-wideband from 2.56 GHz to 12.38 GHz.

2.2.2. Influence of Antenna Feed width (W_2) Modification

An antenna must have proper impedance matching in order to work effectively. An appropriate feed width must be determined for the microstrip line to achieve a 50 Ω impedance. As the feed width varies between 2.5 mm and 3.5 mm, a shift in the frequency range where $S_{11} < -10$ dB was observed across frequencies from 2.56 GHz to 12.38 GHz. For a 3 mm feed width, the return loss reached -68.31 dB at 11.32 GHz and -37.48 dB near 3 GHz, while at 8 GHz, the return loss was -31.99 dB, as shown in Figure 3(c). Therefore, a feed width of 3 mm resulted in the best return loss of -68.31 dB at 11.32 GHz for providing a UWB from 2.56 GHz to 12.38 GHz.

3. OPTIMIZING USING A MACHINE LEARNING ALGORITHM

Machine learning (ML) is employed for estimating the suggested antenna's S-parameters. We can significantly decrease the number of simulations required via machine learning, saving time and minimizing errors. The proposed antenna's performance depends on factors such as the outer and inner radii of the patch, as well as the feed width. Several ML algorithms, such as K-Nearest Neighbors (KNN), Random Forest (RF), Decision Tree (DT), XG Boost (XG), and Artificial Neural Networks (ANN), are employed with the antenna dataset [20, 21, 23]. This dataset is created using CST software by adjusting different input parameters. A total of 708,969 data samples are created with various configurations.

The collection of data has been divided into 20% to be evaluated to assess the performance of the ML models and 80% for learning. To measure accuracy, various error metrics such as Mean Square Error (MSE), Mean Absolute Error (MAE), and R^2 Score are calculated, which are presented in Table 1. The predicted vs. actual results of various ML models are shown in Figure 4. The training time, testing time, and accuracy of each model are depicted in Figure 5. Figure 6(a) shows the error calculation for all configurations. A comparison of KNN, DT, RF, XG Boost, and ANN with CST simulation results is shown in Figure 6(b). Figures 4, 6(a), and Table 1 clearly show that KNN achieved the highest accuracy among all the ML models.

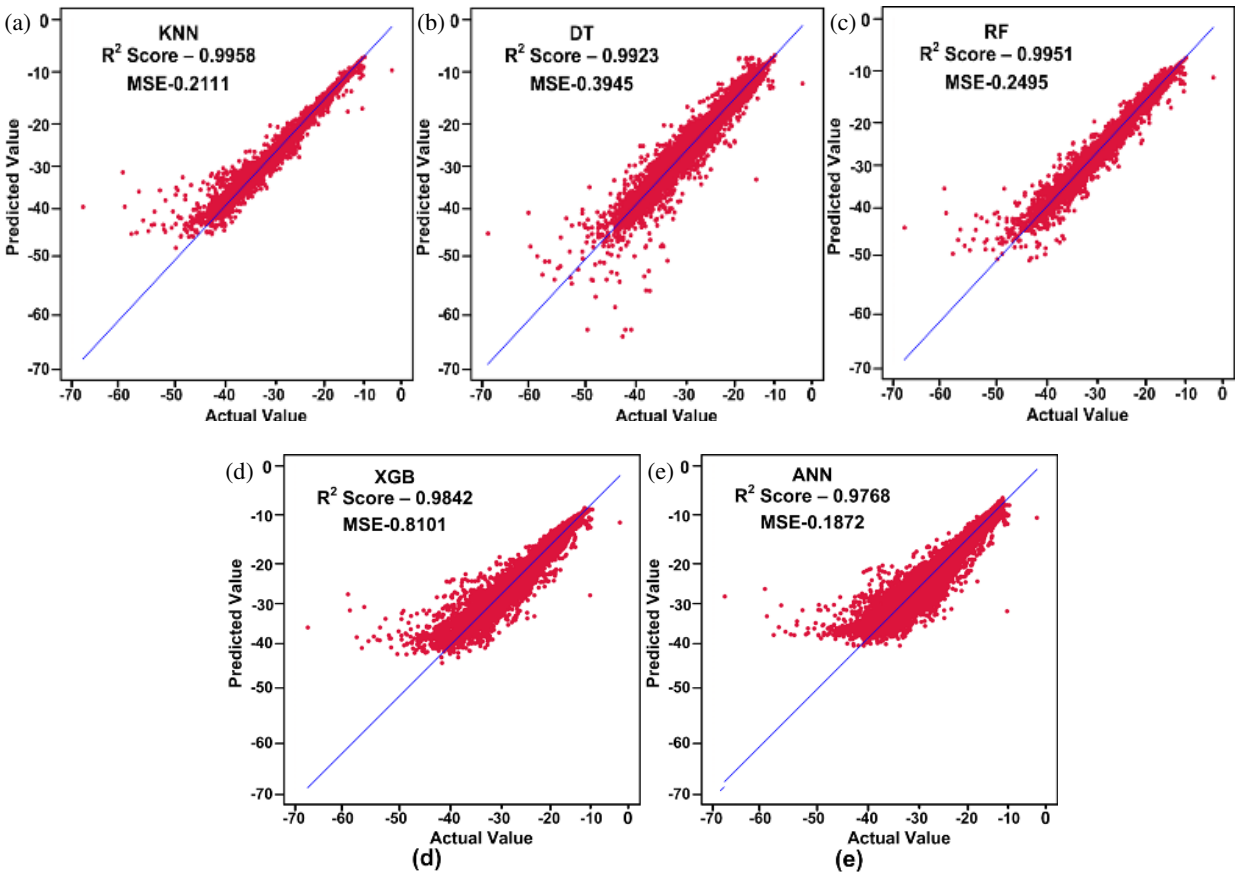

FIGURE 4. Predicted vs Actual values of different ML algorithms.

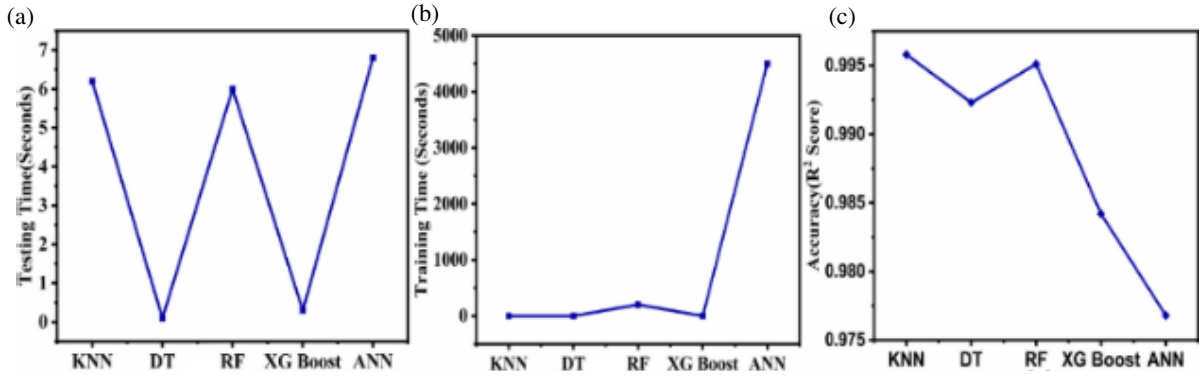

FIGURE 5. (a) Different ML algorithm's testing time, (b) training time and (c) accuracy (R^2 Score).

TABLE 1. MSE, MAE and R2 scores of various ML algorithms.

ML Algorithm	MSE	MAE	R^2 Score
KNN	0.2111	0.1332	0.9958
DT	0.3945	0.2031	0.9923
RF	0.2495	0.1829	0.9951
XG boost	0.8101	0.4045	0.9842
ANN	1.1872	0.5836	0.9768

4. RESULT ANALYSIS AND DISCUSSION

4.1. Return Loss (S_{11})

In Figures 7(a) & (b), the fabricated prototype is exhibited, which is used to verify the predicted result. Figure 8(c) depicts the return loss of the measured and simulated antennas. A wide range of measured impedance bandwidth from 131.45% (2.56 GHz to 12.38 GHz) for return loss $(S_{11}) < -10$ is indicated in the measured result. The measured antenna's S-parameter shows outstanding consensus with the predicted results, indicating that the calculations were accurate. There is a

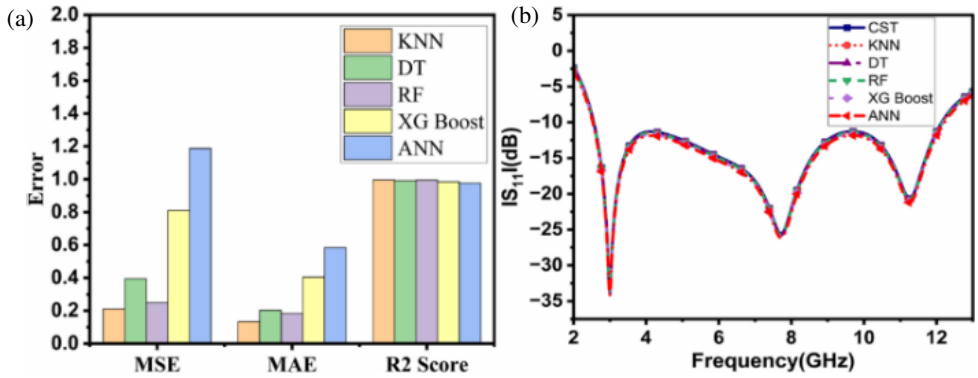

FIGURE 6. (a) Error analysis for different ML algorithms. (b) Comparison of S_{11} between CST and different ML algorithms.

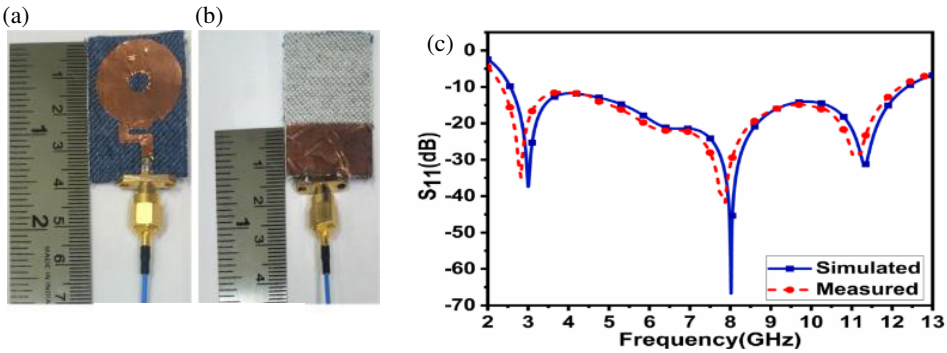

FIGURE 7. Fabricated design. (a) Top view. (b) Bottom view. (c) Simulated and measured S_{11} of the proposed antenna.

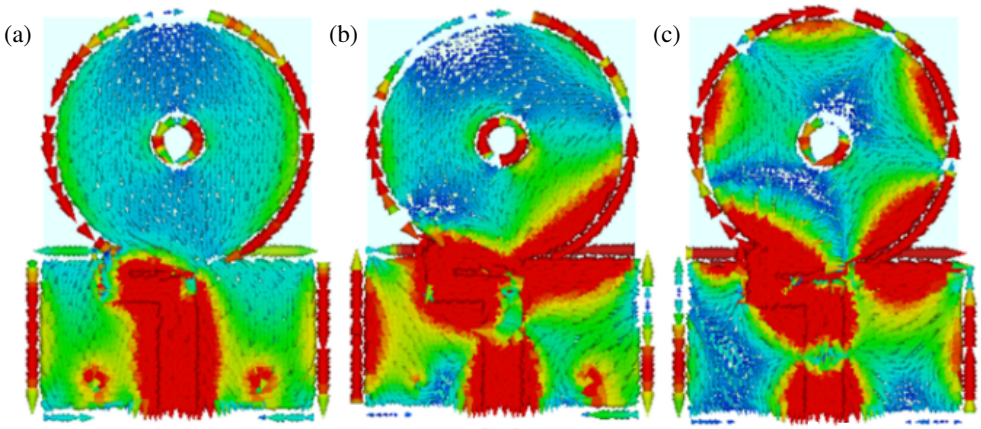

FIGURE 8. The surface current distributions (a) at 3 GHz, (b) at 8 GHz, and (c) at 11.32 GHz.

significantly lower difference between the simulation and examined outcomes in S_{11} at 8 GHz, and it occurs due to the non-uniformity of the substrate, insertion loss, and fabrication methods.

4.2. Surface Current

At 3 GHz, the surface current is primarily concentrated along the edges of the radiating patch and feedline, signifying the excitation of the fundamental resonant mode. This distribution is relatively uniform and symmetrical, indicating effective impedance matching and efficient radiation with minimal reactive losses. At 8 GHz, the current begins to exhibit more complex and localized paths across the patch, forming distinct current loops and regions of high current density. These features are characteristic of the excitation of higher-order modes, which enhance the overall impedance bandwidth and support multi-resonant behaviour. The increase in mode complexity at this frequency demonstrates the antenna's capability to maintain stable performance across a wide operational range. At 11.32 GHz, the surface current becomes highly concentrated near the corners and edges of the radiating patch, while nulls appear in the central region. This distribution is a clear indica-

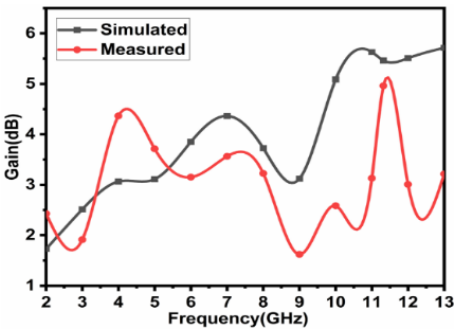

FIGURE 9. Gain versus frequency plot of ring-shaped UWB antenna.

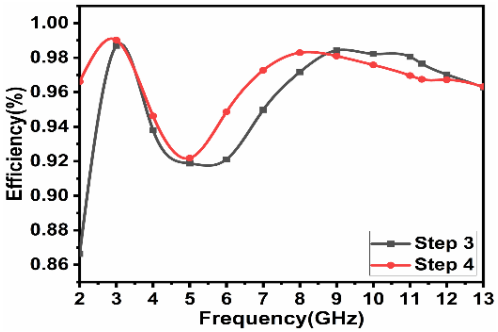

FIGURE 10. Comparison of simulated step 3 versus step 4 efficiency of ring-shaped UWB antenna.

tor of higher-order resonant mode excitation, allowing efficient radiation at the upper end of the antenna's frequency range. Additionally, it can be observed that as the operating frequency increases, the current density intensifies, particularly at the patch extremities. This increase in surface current density contributes to a stronger radiation field, which in turn leads to an improvement in antenna gain. The progression of current distribution with frequency demonstrates the antenna's ability to operate efficiently over a broad spectrum, making it suitable for wideband or multiband wireless applications.

4.3. Analysis of Gain and Efficiency

Figure 9 shows the difference between the UWB antenna's measured and simulated gains. The simulated gains at frequencies 3, 8, and 11.32 GHz are 2.51, 3.70, and 5.46 dBi, respectively. Therefore, the maximum gain of 5.46 dBi occurs at a higher frequency of 11.32 GHz. While the measured gains at frequencies 3, 8, and 11.32 GHz are 1.91, 3.22, and 4.96 dB, respectively, which shows a great match between the predicted and evaluated gains of the UWB antenna. It offers a maximum radiation efficiency of 99% at the lower band. Figure 10 compares simulated radiation efficiencies for Step 3 and Step 4, showing that Step 4 performs better at lower and mid frequencies, while Step 3 shows slightly higher efficiency at 11.32 GHz.

4.4. Radiation Pattern

The antenna's radiation pattern was measured in an anechoic chamber and is shown in Figure 11 for 3, 8, and 11.32 GHz. Co- and cross-polarizations were analyzed in the E (XZ) and H (YZ) planes, showing excellent agreement between simulated and measured results. The realized gain ranges from 2.51 to 5.46 dBi, with radiation efficiency between 96.71% and 99%. At 3 GHz, the cross-polarization in the x-z plane was 44.82 dB lower than the co-polarization, and the same difference was observed in the y-z plane across the entire frequency range. At 8 GHz, the cross-polarization was 43.52 dB lower than the co-polarization in both the x-z and y-z planes. At 11.32 GHz, the cross-polarization was 52 dB lower than the co-polarization in the x-z plane, and this 51.67 dB difference remained consistent in the y-z plane throughout the frequency range. Figure 11 shows a strong match between the antenna's measured and simulated radiation patterns in the E and H planes. The IoT applications typically need an omnidirectional radiation pattern, and these results indicate that the diversity antenna has an omnidirectional radiation pattern, making it ideal for IoT applications.

Although the proposed antenna demonstrates strong performance in terms of bandwidth, gain, flexibility, and SAR compliance, certain limitations exist. SAR analysis was limited to simulations, as experimental measurement is time-intensive (24–48 hours per operating frequency) and impractical for extended testing on human subjects. Additionally, while machine learning significantly reduced simulation efforts, its effectiveness is dependent on the quality and diversity of the dataset, which may restrict its applicability to other antenna geometries.

5. INVESTIGATING ANTENNA PERFORMANCE IN WEARABLE APPLICATIONS

5.1. Bending of Antenna

The UWB antenna is bent across several cylindrical radiuses (R) in mm at 30, 50, 70, and 90 around the Y-axis, as shown in Figure 12(a), in order to measure the bending. The selected radius corresponds to typical human body parts like wrist, forearm, leg, calf, and thigh. Antenna performance is determined by examining how bending affects the return loss. When the antenna is bent, its resonant frequency shifts toward lower values due to the increased effective length. Figure 12(b) shows nonlinear frequency variations from 2.56 to 12.38 GHz with increasing bending radius, resulting from multiple bending-induced effects on return loss (S_{11}). Bending alters the gap between the feed line and ground, affects impedance matching, and deforms the ground structure, changing current distribution. These combined effects make the return loss behavior difficult to predict. Despite nonlinear frequency shifts, the impedance bandwidth in the targeted frequency range remains stable, with no significant changes in center frequencies compared to the flat condition.

5.2. Performance Analysis on the Human Body

Textile antennas, with a thin profile and low dielectric constant $(\varepsilon_r = 1.7)$, offer improved impedance matching and reduced surface wave losses. Unlike rigid antennas, they adapt well to

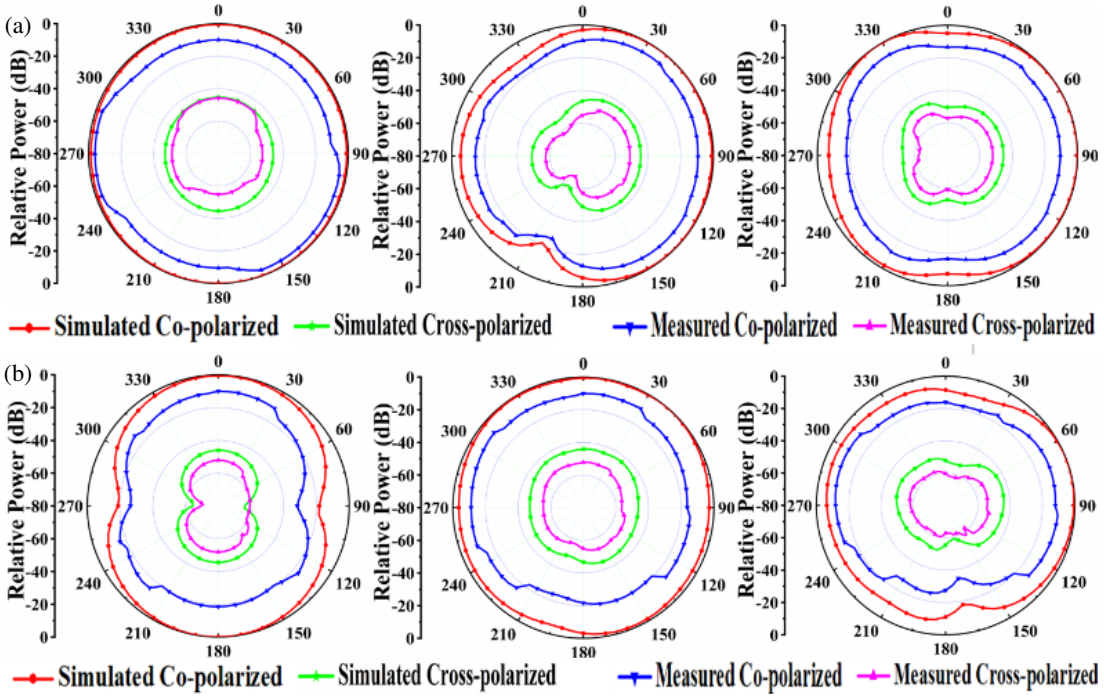

FIGURE 11. Radiation pattern at 3 GHz, 8 GHz, and 11.32 GHz for (a) E plan, (b) H plan.

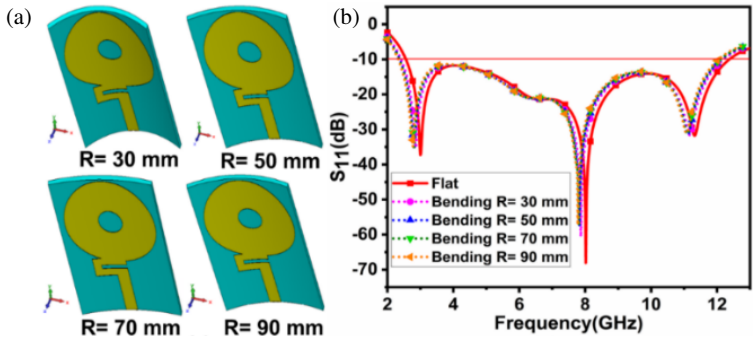

FIGURE 12. (a) Bending of ring-shaped UWB antenna in the Y-axis and (b) comparison of flat and bent antennas at various radius.

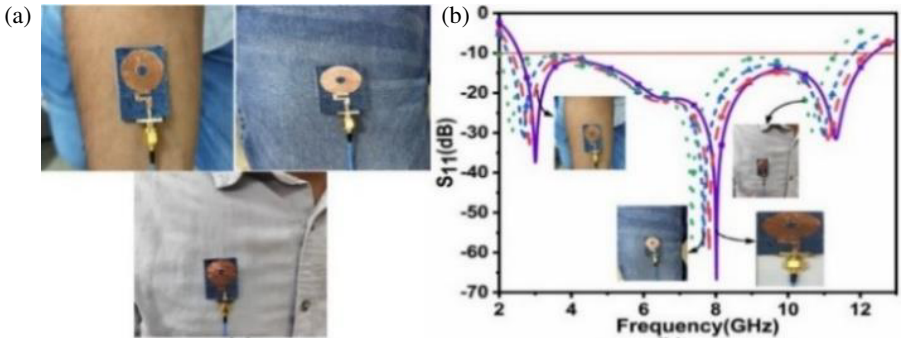

FIGURE 13. (a) Antenna measurement and (b) comparison of the proposed antenna's S_{11} in free space with different human body parts.

body contours and varying tissue properties. However, antenna performance degrades due to radiation absorption by lossy biological tissues of the human body. As shown in Figure 13(a), the antenna was tested on various body parts, hand, chest, and leg, and compared to its performance in free space at operating frequencies of 3, 8, and 11.32 GHz.

Figure 13(b) reveals slight differences in return loss between free space and on-body conditions, indicating frequency detuning. The 3 GHz frequency shifted to 3.34, 3.49, and 3.52 GHz on different body parts. Similarly, the 8 GHz and 11.32 GHz frequencies also shifted to these values. Despite minor increases in return loss, the antenna maintains its ultra-wide band-

TABLE 2. Relative permittivity, conductivity and mass density of tissue model.

Freq.	Tissue	Relative Perm. (ε_r)	Conductivity (S/m)	Density (kg/m^3)
At 3 GHz	Skin	37.45	1.74	1001
	Fat	5.22	2.46	900
	Muscle	52.05	2.14	1006
At 8 GHz	Skin	33.18	5.82	1001
	Fat	4.76	0.44	900
	Muscle	45.49	7.79	1006
At 11.32 GHz	Skin	29.99	9.54	1001
	Fat	4.50	0.68	900
	Muscle	40.98	12.56	1006

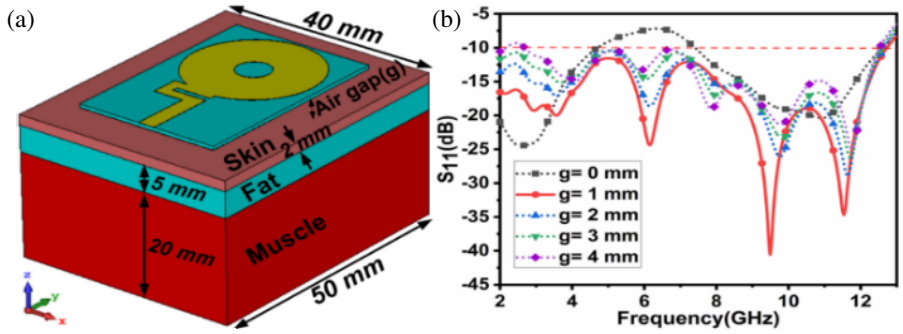

FIGURE 14. (a) 3D Phantom model (b) Comparison of simulated S_{11} for variation of the air gap (g) on phantom.

width of 9.82 GHz, confirming stable on-body performance across conditions.

5.3. On-Phantom Results

Human tissues exhibit higher conductivity at radio frequencies than at DC due to their fluid content. Antenna performance near the body, including bandwidth and gain, is significantly affected. A three-layer body phantom in CST simulates human anatomy, with an adjustable air gap (g) introduced to replicate clothing effects. The phantom, sized 50×40 mm, consists of layers representing 2 mm of skin, 5 mm of fat, and 20 mm of muscle, as shown in Figure 14(a). The electrical properties of these layers at 3, 8, and 11.32 GHz are provided in Table 2. The S_{11} performance of the antenna was analyzed using CST simulation, with the air gap (g) varied between 1 and 4 mm. As illustrated in Figure 14(b), the antenna demonstrates optimal return loss and the widest impedance bandwidth when the air gap between the antenna and body phantom is maintained at 1 mm. This result highlights the critical role of proximity between the antenna and human body in determining electromagnetic performance. Human tissues, particularly muscle, have high water and electrolyte content, making them highly conductive at radio frequencies (RF). When the antenna is positioned too close to these tissues, especially within 1–2 mm, it undergoes strong electromagnetic coupling with the lossy medium. At an air gap of 1 mm, this coupling is balanced: it ensures sufficient interaction with the body for wearable applications while avoiding excessive dielectric loading or energy absorption. As the air gap increases beyond 1 mm (e.g., 2–4 mm), the dielectric influence of the body decreases, leading to impedance mismatches, detuned resonances, and degraded return loss. On the other hand, when the air gap is reduced to 0 mm, i.e., the antenna is in direct contact with the phantom, excessive loading from high-permittivity, high-loss tissues causes a reduction in bandwidth and radiation efficiency. Therefore, maintaining an optimal 1 mm gap offers a practical solution in wearable scenarios.

5.4. SAR Analysis

Specific Absorption Rate (SAR), expressed in watts per kilogram (W/kg), quantifies the rate at which electromagnetic energy is absorbed by biological tissues when they are exposed to RF fields. To ensure user safety, regulatory agencies such as the Federal Communications Commission (FCC) have established SAR exposure limits, 1.6 W/kg for 1 g of tissue and 2.0 W/kg for 10 g of tissue, along with standardized procedures for SAR evaluation [15, 24]. SAR is calculated using the following equation.

$$\mathrm{SAR} = \frac{\sigma |E|^2}{\rho} \tag{2}$$

where σ is the electrical conductivity of the tissue (S/m), E the root mean square (RMS) electric field (V/m), and ρ the tissue density (kg/m^3). To evaluate SAR, a three-layer human

TABLE 3. Comparison of simulated vs measured gain, bandwidth, and SAR.

Freq. (GHz)	Gain		Bandwidth		SAR
	Sim.	Meas.	Sim	Meas.	Sim. (1 g/10 g)
3	2.51	1.91	9.82	9.73	0.605/0.26
8	3.70	3.22			0.842/0.248
11.32	5.46	4.96			0.793/0.263

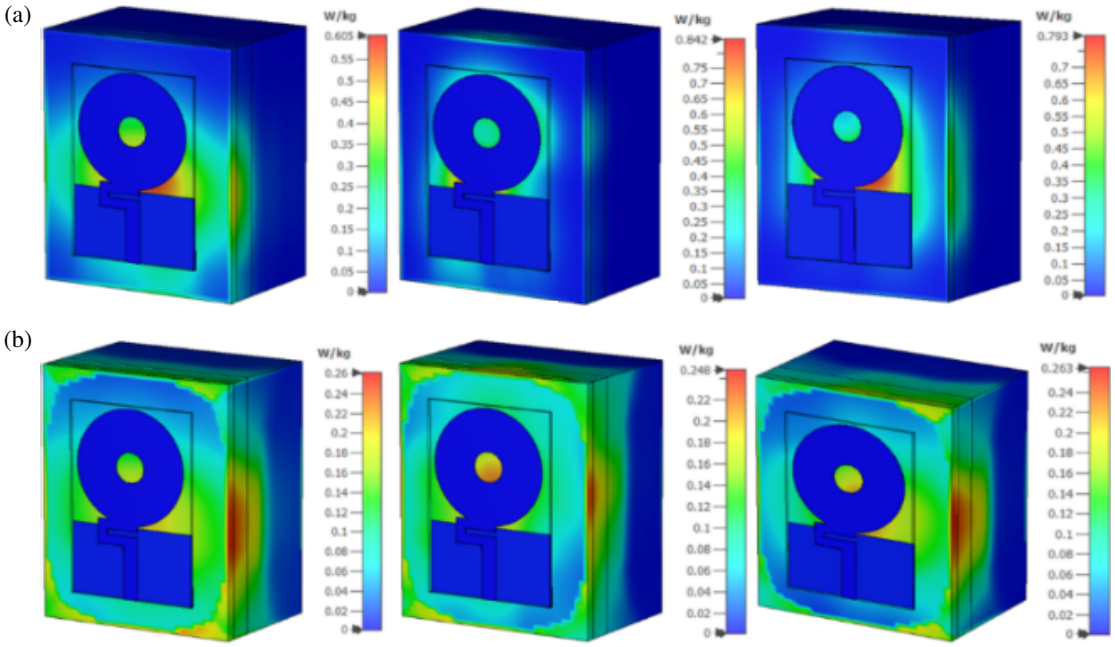

FIGURE 15. SAR values at 3, 8, and 11.32 GHz for (a) 1 g and (b) 10 g.

TABLE 4. Comparison of the proposed work with the existing reported literature.

Ref. No.	Dimension (mm^3)	Sub. Mat.	Oper. Fre. Band (GHz)	Bandwidth (GHz)	Peak Gain	SAR (W/kg) for 1 g/10 g	Machine Learning
[15]	$35.5 \times 30.5 \times 1$	PDMS	3.1–10.42	7.32	NR	NR/0.66, 0.53, 0.90	Yes
[19]	$45 \times 55 \times 1$	PET	3.19–9.30	6.11	2.49	NR	No
[22]	$97 \times 88 \times 1$	Felt	3.4–10.2	6.8	1.9	NR	No
[24]	$20 \times 30 \times 1.4$	Jeans	2.85–9.81	6.96	3.28	1.3/NR	No
[25]	$27.8 \times 23.8 \times 1$	Jeans	3–13	10	5	NR	No
[26]	$43 \times 40 \times 2$	Denim	1.8–10	8.2	5.09	NR	No
[27]	$30 \times 35 \times 1.2$	Denim	3.2–11.8	8.6	3.61, 486	NR	No
This work	**$38 \times 26 \times 0.7$**	**Jean's**	**2.56–12.38**	**9.82**	**5.46**	**0.605, 0.842, 0.793/ 0.26/0.248/0.263**	**Yes**

*NR- Not Reported

body phantom was modeled in CST Microwave Studio to approximate human anatomy. The phantom consists of 2 mm of skin, 5 mm of fat, and 20 mm of muscle, resulting in a total size of $50 \times 40 \times 27\,mm^3$, as illustrated in Figure 13(a). An adjustable air gap (g) was introduced between the antenna and phantom to emulate real-world wearable conditions such as the presence of clothing. For SAR analysis, an optimal air gap of 1 mm was maintained between the antenna and phantom during simulation. The electrical properties — including relative permittivity, conductivity, and density — of each tissue layer at 3, 8, and 11.32 GHz are listed in Table 2. SAR simulations were performed using CST's time-domain solver with adaptive mesh

refinement enabled to enhance accuracy, particularly around tissue boundaries and high-field regions. A hexahedral mesh structure was used to maintain consistency and efficiency in the simulation. SAR values were computed according to IEEE/IEC 62704-1 and FCC standards, for both 1 g and 10 g of tissue, under an input power of 5 mW. The simulated average SAR values at 3, 8, and 11.32 GHz are 0.605, 0.842, and 0.793 W/kg for 1 g tissue, and 0.26, 0.248, and 0.263 W/kg for 10 g tissue, all well below the FCC limits of 1.6 W/kg and 2 W/kg, respectively, as shown in Figures 15(a) and 15(b). Therefore, it makes the ring-shaped UWB antenna for wearable applications.

Table 3 presents a comparison of simulated and measured results for gain, bandwidth, and SAR. It is important to note that SAR values are based solely on simulation, as practical measurement is highly time-consuming, typically requiring 24–48 hours per frequency point, and is not feasible for extensive on-body testing scenarios. Table 4 shows the comparison of the proposed work with the existing reported literature. The proposed antenna offers a wide bandwidth of 9.82 GHz, high gain 5.46 dBi, and compact size using a jeans-based flexible substrate. It is one of the few designs with detailed SAR analysis for 1 g and 10 g tissues, ensuring user safety. Additionally, it uniquely employs machine learning techniques for performance optimization, making it superior to most existing designs in the literature.

6. CONCLUSION

This study presents a compact and flexible ring-shaped UWB textile antenna. A C-type stub is integrated into the design, while a circular slot is removed from the radiator to improve impedance bandwidth. The suggested antenna has a broad impedance bandwidth and a maximum gain of 5.46 dBi, covering frequencies from 2.56 GHz to 12.38 GHz, 131.45% of its center frequency range. Bending analysis was conducted on various human body parts, and it was found that all the results showed good agreement, and an omnidirectional radiation pattern was found. Also, no effect on ultra-wideband arises. Additionally, SAR analysis was conducted to assess how the antenna's radiation affects the human body. At frequencies of 3 GHz, 8 GHz, and 11.32 GHz, the SAR values for 1 g of tissue were 0.605, 0.842, and 0.793 W/kg, and for 10 g of tissue, they were 0.26, 0.248, and 0.263 W/kg. These values are well below the FCC safety limits, 1.6 W/kg for 1 g of tissue and 2 W/kg for 10 g. KNN machine learning algorithm gave the most accurate results and correctly predicted S-parameters of the proposed antenna. KNN achieved higher accuracy 99.58% than all other ML models. Hence, the proposed antenna is suitable for wearable IoT applications.

7. FUTURE WORK

Future work will focus on improving the real-world applicability and deployment of the proposed flexible UWB antenna. A primary direction involves the real-time implementation of machine learning models on embedded platforms or edge devices to enable rapid and energy-efficient antenna performance prediction, thereby reducing dependence on full-wave electromagnetic simulations. Furthermore, the mechanical durability of the antenna will be experimentally evaluated under repeated bending, folding, and washing conditions to assess its robustness in wearable environments. Analyzing any potential performance degradation will help determine long-term reliability. In addition, integration into a complete IoT hardware platform will facilitate end-to-end performance evaluation in practical scenarios such as health monitoring, activity tracking, and wireless body area networks (WBANs), bridging simulation and practical realization.

REFERENCES

[1] Kaur, I., B. Basu, A. K. Singh, V. Rishiwal, S. Tanwar, G. Sharma, P. N. Bokoro, and R. Sharma, "Annular ring ultra wideband antenna integrated with metallic via array for IoT applications," *IEEE Access*, Vol. 10, 73 446–73 457, 2022.

[2] Kirtania, S. G., B. A. Younes, A. R. Hossain, T. Karacolak, and P. K. Sekhar, "CPW-fed flexible ultra-wideband antenna for IoT applications," *Micromachines*, Vol. 12, No. 4, 453, 2021.

[3] Oni, M. A. I. and M. T. Ali, "Design of a compact, low-profile, elliptical patch UWB antenna and performance analysis in vicinity of human layered tissue model for wireless body area network (WBAN) applications," *International Journal of Innovation and Applied Studies*, Vol. 8, No. 4, 1770–1781, 2014.

[4] Mishra, A., P. S. Kumar, R. Shrestha, K. Malathi, and K. V. P. Kumar, "Design and analysis of compact diversity antenna for wearable applications," in *Journal of Physics: Conference Series*, Vol. 1964, No. 6, 062033, 2021.

[5] Yan, S., L. A. Y. Poffelie, P. J. Soh, X. Zheng, and G. A. E. Vandenbosch, "On-body performance of wearable uwb textile antenna with full ground plane," in *2016 10th European Conference on Antennas and Propagation (EuCAP)*, 1–4, Davos, Switzerland, 2016.

[6] Yadav, A., V. K. Singh, A. K. Bhoi, G. Marques, B. Garcia-Zapirain, and I. de la Torre Díez, "Wireless body area networks: UWB wearable textile antenna for telemedicine and mobile health systems," *Micromachines*, Vol. 11, No. 6, 558, 2020.

[7] Karad, K. V. and V. S. Hendre, "A flower bud-shaped flexible UWB antenna for healthcare applications," *EURASIP Journal on Wireless Communications and Networking*, Vol. 2023, No. 1, 27, 2023.

[8] Kumar, V., S. Kumar, and B. Gupta, "Performance analysis of swastika slot UWB antenna in vicinity of dispersive human layered tissue model," in *2014 IEEE REGION 10 SYMPOSIUM*, 219–223, Kuala Lumpur, Malaysia, Apr. 2014.

[9] Sesha Vidhya, S., S. R. Devi, and K. G. Shanthi, "Design trends in ultra wide band wearable antennas for wireless On-body networks," *ARPN Journal of Engineering and Applied Sciences*, Vol. 12, No. 9, 2782–2790, 2017.

[10] Ali, E. M., W. A. Awan, M. S. Alzaidi, A. Alzahrani, D. H. Elkamchouchi, F. Falcone, and S. S. M. Ghoneim, "A shorted stub loaded UWB flexible antenna for small IoT devices," *Sensors*, Vol. 23, No. 2, 748, 2023.

[11] Khan, M. M. and A. Sultana, "Novel and compact ultra-wideband wearable band-notch antenna design for body sensor networks and mobile healthcare system," *Engineering Proceedings*, Vol. 3, No. 1, 1, 2020.

[12] Lin, X., Y. Chen, Z. Gong, B.-C. Seet, L. Huang, and Y. Lu, "Ultrawideband textile antenna for wearable microwave medical imaging applications," *IEEE Transactions on Antennas and Propagation*, Vol. 68, No. 6, 4238–4249, 2020.

[13] Pandey, U., P. Singh, R. Singh, N. P. Gupta, S. K. Arora, and E. Nizeyimana, "Miniaturized ultrawideband microstrip antenna for IoT-based wireless body area network applications," *Wireless Communications and Mobile Computing*, Vol. 2023, No. 1, 3950769, 2023.

[14] Vignesh, N. A., R. Kumar, R. Rajarajan, S. Kanithan, E. S. Kumar, A. K. Panigrahy, and S. Periyasamy, "Silicon wearable body area antenna for speech-enhanced IoT and nanomedical applications," *Journal of Nanomaterials*, Vol. 2022, No. 1, 2842861, 2022.

[15] Praveena, A., G. Umamaheswari, J. K. Rai, and P. Ranjan, "Machine learning enabled compact flexible full ground UWB antenna for wearable applications," *International Journal of Microwave and Wireless Technologies*, Vol. 16, No. 8, 1303–1315, 2024.

[16] Desai, A., H.-T. Hsu, B. M. Yousef, A. M. Ameen, Y.-F. Tsao, and A. A. Ibrahim, "UWB connected ground transparent 4-port flexible MIMO antenna for IoT applications," *IEEE Internet of Things Journal*, Vol. 11, No. 7, 12 475–12 484, 2024.

[17] Lakrit, S., S. Das, S. Ghosh, and B. T. P. Madhav, "Compact UWB flexible elliptical CPW-fed antenna with triple notch bands for wireless communications," *International Journal of RF and Microwave Computer-Aided Engineering*, Vol. 30, No. 7, e22201, 2020.

[18] Das, S., H. Islam, T. Bose, and N. Gupta, "Ultra wide band CPW-fed circularly polarized microstrip antenna for wearable applications," *Wireless Personal Communications*, Vol. 108, 87–106, 2019.

[19] Balanis, C. A., *Antenna Theory: Analysis and Design*, 3rd ed., John Wiley & Sons, 2016.

[20] Rai, J. K., S. Pandey, P. Ranjan, R. Chowdhury, A. Sharma, and G. Das, "High-gain triple-band T-shaped dielectric resonator based hybrid two-element MIMO antenna for 5G new radio, Wi-Fi 6, V2X, and C-band applications with a machine learning approach," *International Journal of Communication Systems*, Vol. 38, No. 5, e6038, 2025.

[21] Rai, J. K., U. Patel, P. Tiwari, P. Ranjan, and R. Chowdhury, "Machine learning enabled compact frequency-tunable triple-band hexagonal-shaped graphene antenna for THz communication," *International Journal of Communication Systems*, Vol. 38, No. 1, e6044, 2025.

[22] Samal, P. B., P. J. Soh, and G. A. E. Vandenbosch, "UWB all-textile antenna with full ground plane for off-body WBAN communications," *IEEE Transactions on Antennas and Propagation*, Vol. 62, No. 1, 102–108, 2014.

[23] Ranjan, P., A. Maurya, H. Gupta, S. Yadav, and A. Sharma, "Ultra-wideband CPW fed band-notched monopole antenna optimization using machine learning," *Progress In Electromagnetics Research M*, Vol. 108, 27–38, 2022.

[24] Chen, P., D. Wang, and Z. Gan, "Flexible and small textile antenna for UWB wireless body area network," *Micromachines*, Vol. 14, No. 4, 718, 2023.

[25] Khan, M. M., B. Yeboah-Akowuah, K. Islam, E. T. Tchao, S. Bhattacharyya, R. Dey, M. Masud, and F. Alraddady, "Novel design of UWB jeans based textile antenna for body-centric communications," *Computer Systems Science & Engineering*, Vol. 42, No. 3, 1079–1093, 2022.

[26] Chilukuri, S. and S. Gogikar, "A CPW fed denim based wearable antenna with dual band-notched characteristics for UWB applications," *Progress In Electromagnetics Research C*, Vol. 94, 233–245, 2019.

[27] Tiwari, B., S. H. Gupta, and V. Balyan, "Investigation on performance of wearable flexible on-body ultra-wideband antenna based on denim for wireless health monitoring," *Journal of Electronic Materials*, Vol. 50, 6897–6909, 2021.